IEEE Access
Multidisciplinary | Rapid Review | Open Access Journal

Received 23 March 2024, accepted 2 April 2024, date of publication 10 April 2024, date of current version 19 April 2024.

Digital Object Identifier 10.1109/ACCESS.2024.3387369

RESEARCH ARTICLE

Distributed Model Predictive Frequency Control of Inverter-Based Power Systems

MARC MORITZ[1], TOBIAS HEINS[1], SRIRAM KARTHIK GURUMURTHY[1], (Graduate Student Member, IEEE), MARTINA JOŠEVSKI[1], (Member, IEEE), ILKA JAHN[1,2], (Member, IEEE), AND ANTONELLO MONTI[1,3], (Senior Member, IEEE)

[1]Institute for Automation of Complex Power Systems, E.ON Energy Research Center, RWTH Aachen University, 52074 Aachen, Germany
[2]School of Electrical Engineering and Computer Science (EECS), KTH Royal Institute of Technology, 100 44 Stockholm, Sweden
[3]Fraunhofer FIT, 53757 Sankt Augustin, Germany

Corresponding author: Marc Moritz (marc.moritz@eonerc.rwth-aachen.de)

The work of Marc Moritz and Ilka Jahn was supported by the Excellence Strategy of German Federal Government and the Länder (Junior Principal Investigator Grant at RWTH Aachen). The work of Tobias Heins, Sriram Karthik Gurumurthy, Martina Joševski, and Antonello Monti was supported by German Research Foundation-Deutsche Forschungsgemeinschaft (DFG) under Grant 432169785.

ABSTRACT The increasing dominance of inverter-based resources (IBRs) in power generation leads to significantly faster frequency dynamics in modern power systems. Therefore, the secondary control within the classical hierarchical structure must operate significantly faster. However, high communication burdens are inherent to centralized implementations of secondary control. This paper proposes a faster, distributed model predictive control (MPC) scheme for secondary frequency control of inverter-based power systems. The controller predicts the IBRs' local frequency dynamics by considering the impact of the primary control of nearby IBRs. To obtain an optimal model-predictive control problem consisting of distributable subproblems, we introduce a novel trimming procedure to the frequency divider concept, an analytical formulation that estimates the local frequency at system buses. These subproblems have a tunable degree of mutual coupling. The presented distributed MPC achieves fast, error-free frequency regulation in the presence of abrupt load changes while also being robust to communication losses of participating IBRs. By design, the distributed control relies on a sparse neighbor-to-neighbor communication structure and uses local MPC problems that do not scale in complexity with system size. Numerical simulations of the IEEE 39-bus system and an extended CIGRE medium voltage power system demonstrate the fast performance of the proposed distributed MPC scheme for secondary frequency control.

INDEX TERMS Distributed control, frequency divider, model predictive control, secondary frequency control, inverter-based resources.

I. INTRODUCTION

In the current energy transition, renewable energy resources such as photovoltaic and wind power installations are distributedly integrated into all parts of the electrical grid. Such distributed resources are typically interfaced with the grid via an inverter, which can be classified into grid-following and grid-forming types [1], the latter being a promising solution to provide an inertial response and primary frequency control.

The associate editor coordinating the review of this manuscript and approving it for publication was Pinjia Zhang.

In general, the integration of inverter-based resources (IBRs) and reduction of rotational inertia leads to faster frequency and voltage dynamics in the modern power system. This raises the need to revisit and rethink the classical hierarchical control structures to maintain power system stability [2]. In this paper, we focus on the secondary frequency control utilizing solely grid-forming IBRs.

Several secondary frequency control approaches for are proposed in the literature, ranging from centralized to decentralized. Centralized methods include the proportional-integral (PI)-based automatic generation control (AGC),

which is used in conventional power systems, as well as robust control methods and model predictive control (MPC) [3]. A centralized controller collects the information of all distributed generation units to calculate a control signal and sends it to the local primary controllers of each generation unit. Due to the nature of their structure, centralized controllers require an extensive communication network and represent a single point of failure [4]. In decentralized frequency control, local controllers at each generation unit aim to restore the grid frequency. Decentralized approaches often rely on a separation of time scales between the fast primary control and the secondary control dynamics and, therefore, are slower than other methods [5]. A general disadvantage of decentralized control is that the local controllers do not coordinate their actions which might lead to them working against one another [6].

To avoid the drawbacks of both centralized and decentralized control, distributed control approaches are proposed in which local controllers at each generation unit use local information and neighbor-to-neighbor communication to perform secondary frequency control cooperatively, as in [5]. In [5], local PI controllers coordinate their control actions utilizing a distributed averaging procedure. However, disadvantages of PI control are that it cannot inherently deal with operational constraints, such as the active power limit of each IBR and that is has a slower response compared to modern control methods. In contrast, MPC leverages a model-based prediction of the system's dynamic behavior to achieve a fast control response, is capable of considering system constraints, and is well suited for multiple-input and multiple-output (MIMO) systems [7]. Therefore, MPC can provide better frequency responses than PI control and include multiple control objectives [8].

Several distributed MPC schemes are presented in the literature, combining the advantages of distributed control and MPC. Distributed MPC makes use of parallel computation, which can lead to reduced computation times compared to centralized MPC [9]. Furthermore, distributed MPC has better scalability than centralized MPC since the complexity of each local control problem does not necessarily grow with system size [3]. Reference [10] presents a distributed MPC scheme in which local model predictive controllers coordinate their control actions utilizing a consensus-based algorithm involving neighbor-to-neighbor communication. However, the presented control approach relies on adjusting the load consumption by manipulating the load operating voltages. We consider adjusting the active power output of the generation units to be a more practical approach for frequency control. The distributed MPC in [3] uses a projection-based algorithm to control the frequency via the tie-line power exchange between multiple microgrids. The algorithm relies on an extensive communication structure, where every system bus, including load buses, is required to participate in the control scheme, thus putting a high requirement on the communication and control infrastructure. Feedback linearization is used in [4] to design a distributed MPC for secondary frequency and voltage control. The designed controller considers a high-order model of the local inverter control dynamics. However, the coupling dynamics between the IBRs are not modeled in the control system. Convergence is achieved by averaging the neighboring trajectories in the MPC cost function. In [11], large-scale power systems are decomposed into interconnected subsystems and controlled using a feasible cooperation-based MPC. The generation units within one control area are lumped into a single equivalent generator and are solely synchronous generators. A similar approach is used in [12], where each control area is represented by a single generator, which could be either a hydro unit, thermal plant, or wind farm. The integration of IBRs will, however, lead to significantly faster frequency dynamics. Additionally, it was previously shown in [13] that the frequency is not equal at different system buses during a transient. This, hence, raises the need to control generation units individually. The coupling between the generation units in [11] and [12] is modeled by the tie line power exchange. To control individual generation units, these approaches would require knowledge of the power flow in all lines, which is, on the time scale of a control system, infeasible in a meshed power system.

In this paper, we propose a distributed MPC scheme for secondary frequency control that controls IBRs individually and models the coupling dynamics between them by leveraging the frequency divider theory. The frequency divider formula has been derived in [13], validated through hardware-in-the-loop simulations in [14], and is an analytical formulation to calculate the frequency of load buses during transient events. Initially, the frequency divider was derived for classical power systems based on synchronous generators. However, it has been shown to give accurate results for inverter-based power systems if IBRs provide virtual inertia and Thevenin equivalents are included in the estimation [15]. The formula has been applied for online frequency estimation in [16] and a distributed MPC for multi-area power systems has been designed in [17] based on the Thevenin equivalent representation. The distributed MPC in [17], however, retains a central control unit for each area.

The novelty and contribution of this paper are:

- A distributed MPC scheme that controls IBRs individually via active power setpoints, as compared to approaches using centralized MPC with single-point-of-failure [8], distributed MPC via unpractical load adjustment [10], and distributed MPC assuming slow dynamics that are no longer relevant with IBRs [12].
- A control system architecture that requires communication of each local controller solely with a defined set of neighbors, as compared to approaches that require extensive communication between different buses [3].
- A trimming method for the frequency divider [13] to decompose the global prediction model and optimization problem while keeping physical interpretability.
- Submodels that do not scale with the size of the system. Only local dynamics are described in the prediction

model explicitly, whereas the grid topology is modeled implicitly through the frequency divider calculation based on the grid's admittance matrix.
- The proposed distributed MPC is applicable to any grid topology, particularly meshed grids. The distributed scheme does not rely on tie line power exchanges for decoupling as in [11] and [12].
- Robustness of the distributed MPC to communication losses by utilizing an optimization algorithm that is guaranteed to converge under communication losses.

With the proposed distributed approach based on frequency divider trimming, the intermediate range between centralized and decentralized MPC can be covered without any modifications to the modeling. Numerical simulations verify the performance and robustness of the presented approach.

II. PROBLEM FORMULATION

Distributed control of power system frequency poses challenges because the frequency is controlled locally but has to be synchronized among all generation units in the power system. The interaction between the generators must be considered in the design and operation of distributed frequency control systems to achieve a coordinated system behavior with a fast and stable control response. In this Section, we will state our requirements for distributed frequency control and describe the centralized MPC scheme that forms the base for this work.

A. REQUIREMENTS FOR DISTRIBUTED FREQUENCY CONTROL

Local frequency control of generation units impacts the response of other units and vice versa. Thus, a distributed control scheme requires information on states and control parameters. Due to the significant increase in the number of generation units in the power system, a distributed control scheme should avoid the need for global parameter and state information to limit the dependency on data exchange and the complexity of the control system. Therefore, the distributed MPC developed in this paper should rely on a sparse communication network, i.e., information exchange is only possible with a set of neighboring generation units, which needs to be defined based on the strength of the coupling dynamics. As such, only the parameter and state information of the defined set of neighbors can be included in the prediction model. Furthermore, the proposed solution has to be scalable to ensure its applicability in large power systems.

Distributed model predictive control schemes employ distributed optimization algorithms to solve a common problem. Since we demand a neighbor-to-neighbor communication structure, the distributed optimization must not rely on a central coordination unit. Further, only neighbor-to-neighbor information exchange should be required for the algorithm's convergence. The number of iterations needed to compute a control input has to be limited to guarantee fast execution and reduce the vulnerability to communication delays. Furthermore, the designed MPC should be able to constrain the generation units' frequency dynamics and active power infeed.

Before presenting the proposed solution, we introduce the frequency prediction model that we adopt in this paper and state the optimization problem.

B. PREDICTION MODEL

The prediction of power system frequency response has traditionally been centered around the well-known swing equation [18]. This paper focuses on inverter-based power systems, i.e., no synchronous generators are present. Thus, the frequency response can not be based on the inertial response of synchronous generators but must instead be derived from the primary control strategies of the IBRs. We adopt the grid-forming IBR control configuration, as well as the prediction model derived in [19], which we summarize in this Subsection with its main assumptions.

Each IBR $i \in \mathcal{N}_i = \{1, \ldots, n_i\}$ is modeled with two states, namely their output angular frequency ω_i and their output active power P_i. The IBRs employ a grid-forming droop control strategy with a first-order low-pass filter smoothing out the calculated instantaneous powers. This filter introduces virtual inertia to the IBR dynamics that is proportional to the filter time constant [20], [21]. The frequency droop control law and active power filter are described by

$$\omega_i = \omega_\mathrm{n} - m_{i,\mathrm{p}} \left(P_{i,\mathrm{f}} - P_i^*\right) \tag{1}$$

$$\dot{P}_{i,\mathrm{f}} = \frac{1}{\tau_{i,\mathrm{p}}} \left(P_i - P_{i,\mathrm{f}}\right). \tag{2}$$

Here, ω_n is the system nominal frequency; P_f and P^* are the filtered active power and set-point, respectively. The droop gain is m_p, and τ_p is the filter time constant. Assuming a piecewise constant set-point P^*, the first state equation is obtained from (1) and (2) as

$$\dot{\omega}_i = -\frac{1}{\tau_{i,\mathrm{p}}} \omega_i - \frac{m_{i,\mathrm{p}}}{\tau_{i,\mathrm{p}}} P_i + \frac{m_{i,\mathrm{p}}}{\tau_{i,\mathrm{p}}} P_i^* + \frac{1}{\tau_{i,\mathrm{p}}} \omega_\mathrm{n}. \tag{3}$$

The MPC shall adjust the pre-event active power set-point $P_{0,i}^*$ by setting ΔP_i^*, so that the input to the IBR is defined by

$$P_i^* = P_{0,i}^* + \Delta P_i^*.$$

We envision that $P_{0,i}^*$ is obtained by a higher level control or market mechanism that optimizes the active power scheduling, balances load and generation on a longer time scale, and ensures the availability of reserve power for the primary and secondary control.

While the first state equation (3) describes the IBR frequency dynamics, an additional state equation is derived to describe the output active power modeled as the active power flow over the output inductance X_{ig}. The voltage angle difference is considered small so that $\sin\delta \approx \delta$. Assuming that the impact of active power and frequency dynamics on

the bus voltage is negligible, the active power dynamics are formulated as

$$\dot{P}_i = \frac{V_i V_g}{X_{ig}} \dot{\delta}_{ig}, \tag{4}$$

with the transmission angle dynamics

$$\dot{\delta}_{ig} = \omega_i - \omega_g. \tag{5}$$

The index g denotes the grid side bus of the IBR output inductance.

The frequency divider matrix D is calculated from the systems admittance matrix as described in [13]. Using D, the angular frequency ω_g can be expressed as interpolation of the generator frequencies in the system as

$$\omega_g = D_g \underbrace{\begin{bmatrix}\omega_1 & \dots & \omega_{n_i}\end{bmatrix}^T}_{\omega_\mathrm{G}}. \tag{6}$$

Here, D_g denotes the row of D corresponding to the grid side bus g. The vector ω_G comprises all generator-, i.e., IBR frequencies. From (4), (5), and (6), the second state equation is obtained as

$$\dot{P}_i = \frac{V_i V_g}{X_{ig}} \left(\omega_i - D_g\, \omega_\mathrm{G}\right). \tag{7}$$

The frequency prediction model takes the form of a continuous state-space model

$$\dot{x} = A\,x + B\,u + E\,z \tag{8a}$$
$$y = C\,x \tag{8b}$$

and is composed of (3) and (7) for each IBR. The state, control input, and disturbance vectors are obtained by stacking as

$$x = \{x_i\}_{i=1}^{n_i}, \quad x_i = [\omega_i \quad P_i]^T \tag{9a}$$
$$u = \{u_i\}_{i=1}^{n_i}, \quad u_i = \Delta P_i^* \tag{9b}$$
$$z = \{z_i\}_{i=1}^{n_i}, \quad z_i = [P_{0,i}^* \quad \omega_\mathrm{n}]^T \tag{9c}$$
$$y = \{y_i\}_{i=1}^{n_i}, \quad y_i = \omega_i. \tag{9d}$$

The model (8a)–(8b) assumes constant voltages over the prediction horizon to adopt the LTI property. The IBRs in this paper are equipped with a primary PI voltage control regulating the grid side voltage to 1.0 p.u. In the simulations, bus voltages remain in a 0.9 - 1.11 p.u. band, whereas individual IBR voltages fluctuate by less than 0.06 p.u. during a single transient. This affects the accuracy of the state equation with a good margin below the allowed voltage band. As a result, decoupled and constant voltage control is assumed.

C. CENTRALIZED OPTIMIZATION PROBLEM

This Section defines a centralized optimal control problem (OCP) based on the prediction model. Like the prediction model, the OCP is adopted from our previous work in [19]. The OCP is suited to be solved in a receding horizon fashion by a centralized MPC. After presenting the OCP, we identify its implementation challenges in a distributed MPC framework.

The OCP consists of an objective function, the prediction model, and constraints. When applying MPC, at every time-step k, we solve a finite-time OCP over a prediction horizon H_p. The decision variables are the control inputs over the control horizon H_u. After the optimization problem is solved, only the first control input is applied, and the optimization is repeated using moving horizons at time $k+1$. Hereafter, $\{\cdot\}\,(k+j \mid k)$ refers to the prediction of a variable $\{\cdot\}$ at the future time step $k+j$ given the information available at the time k. The objective function J of the optimization problem is defined as a convex, quadratic function of the form

$$\begin{aligned} &J(u(\cdot \mid k), \epsilon_\omega, \epsilon_{\Delta\omega}, \epsilon_P) \\ &\quad = Q \sum_{j=1}^{H_\mathrm{p}} (y - y_\mathrm{ref})^2\,(k+j \mid k) \\ &\qquad + R \sum_{j=0}^{H_\mathrm{u}-1} \Delta u(k+j \mid k)^2 + S \sum_{j=0}^{H_\mathrm{p}-1} u(k+j \mid k)^2 \\ &\qquad + \rho_1\,\epsilon_\omega^2 + \rho_2\,\epsilon_{\Delta\omega}^2 + \rho_3\,\epsilon_P^2. \end{aligned} \tag{10}$$

Q, R and S represent positive scalar weights while ρ_1, ρ_2 and ρ_3 are the slack variables' weights. The first term in the objective function penalizes deviations of the controlled outputs from their reference trajectories over the prediction horizon H_p. The second and third terms in (10) penalize the changes and absolute values of the control inputs over the control horizon H_u to restrict control action. The remaining terms in the objective function correspond to the quadratically penalized slack variables and assure the feasibility of the optimization problem.

We introduce constraints on the prediction model's states, inputs, and outputs to fully define the OCP. The constraints represent either physical system limitations or requirements for system operation. Firstly, limitations on the active power injection at the IBR buses translate into constraints on the inputs ΔP_i^* and constraints on the second state P_i of each IBR as

$$u_{min} \le u(k+j \mid k) \le u_{max}, \quad j \in \mathbb{N}_{[1,H_\mathrm{u}]} \tag{11}$$
$$x_i^{[2]}\,(k+j|k) \le P_{i,\max} + \epsilon_P, \quad i \in \mathbb{N}_{[1,n_i]},\ j \in \mathbb{N}_{[1,H_\mathrm{p}]} \tag{12a}$$
$$x_i^{[2]}\,(k+j|k) \ge P_{i,\min} - \epsilon_P, \quad i \in \mathbb{N}_{[1,n_i]},\ j \in \mathbb{N}_{[1,H_\mathrm{p}]}. \tag{12b}$$

These constraints impose the limitation of available active power from the primary DC source of the IBR. Further, we constrain the IBRs' output frequencies and rate of change of frequency (RoCoF):

$$y(k+j \mid k) \le \omega_\mathrm{max} + \epsilon_\omega, \quad j \in \mathbb{N}_{[1,H_\mathrm{p}]} \tag{13a}$$
$$y(k+j \mid k) \ge \omega_\mathrm{min} - \epsilon_\omega, \quad j \in \mathbb{N}_{[1,H_\mathrm{p}]} \tag{13b}$$
$$\Delta y(k+j \mid k) \le \Delta\omega_\mathrm{max} + \epsilon_{\Delta\omega}, \quad j \in \mathbb{N}_{[1,H_\mathrm{p}]} \tag{13c}$$
$$\Delta y(k+j \mid k) \ge \Delta\omega_\mathrm{min} - \epsilon_{\Delta\omega}, \quad j \in \mathbb{N}_{[1,H_\mathrm{p}]}, \tag{13d}$$

where $\Delta y(k+j \mid k)$ denotes the difference of frequencies between two consecutive time steps, i.e., $\Delta y(k+j \mid k) = y(k+j \mid k) - y(k+j-1 \mid k)$. The state constraints (12a)

and (12b) include the definition of the frequency divider formula, as (7) connects each IBR's power state P_i with a linear combination of the frequencies at all generation buses. Similarly, the output constraints (13a)–(13d) contain the frequency divider formula, as the outputs are defined as the frequency states of each IBR ω_i. These states are connected to the frequency divider-dependent power states via (3). Hence, the state and output constraints pose coupling constraints that connect states and inputs of all IBRs in the optimization problem. Lastly, the slack variables can only take non-negative values

$$\epsilon_\omega \geq 0, \quad \epsilon_{\Delta\omega} \geq 0, \quad \epsilon_P \geq 0. \tag{14}$$

The centralized OCP can be summarized as

$$\begin{aligned} \min_{u(\cdot|k),\epsilon_\omega,\epsilon_{\Delta\omega},\epsilon_P} \quad & J(u(\cdot \mid k), \epsilon_\omega, \epsilon_{\Delta\omega}, \epsilon_P) \\ \text{s.t.} \quad & \text{disc. system dynamics, i.e.,} \\ & x(k+1) = A_\mathrm{d}x(k) + B_\mathrm{d}u(k) + E_\mathrm{d}z(k) \\ & y(k) = C_\mathrm{d}x(k) \\ & x(k \mid k) = x(k), \\ & \text{input constraints (11), (14),} \\ & \text{state constraints (12a), (12b),} \\ & \text{output constraints (13a)–(13d).} \end{aligned} \tag{15}$$

The resulting OCP in (15) is a convex optimization problem with a quadratic cost function. Hence, it can be represented in quadratic programming (QP) form. We adopt the definitions introduced in [22] and use the notation of a stacked input vector $\mathcal{U}(k)$ to obtain a compact representation of the OCP in QP form

$$\begin{aligned} \min_{\mathcal{U}(k)} \quad & \mathcal{U}^T(k)\,\mathcal{H}\,\mathcal{U}(k) - \mathcal{G}^T(k)\mathcal{U}(k) \\ \text{s.t.} \quad & \Omega\,\mathcal{U}(k) \leq b(k), \end{aligned} \tag{16}$$

where $\mathcal{H}$ and $\mathcal{G}(k)$ represent the Hessian matrix and the gradient vector, respectively, while the matrix Ω and the vector $b(k)$ are defined to combine the constraints (11)–(14) into a single matrix inequality. Unlike $\mathcal{H}$ and Ω, $\mathcal{G}(k)$ and $b(k)$ depend on the time step k. The stacked input vector is defined as

$$\mathcal{U}(k) := \left[u^T(k \mid k) \ \ldots \ u^T(k + H_\mathrm{u} - 1 \mid k)\ \epsilon_\omega\ \epsilon_{\Delta\omega}\ \epsilon_P\right]^T,$$

consisting of all decision variables over the control horizon, including the slack variables.

As discussed, state coupling between the different IBRs in the prediction model is rooted in the frequency divider matrix. The grid bus frequencies of each IBR are stated as an interpolation of all generation frequencies. Hence, each IBR is coupled with all other IBRs. This global state coupling carries over to global coupling of the decision variables in the OCP cost function (10) and in the coupling constraints (12a)–(13d). In particular, each IBR's control input u is coupled with all other IBRs, resulting in a globally cost- and constraint-coupled optimization problem. A reformulation of such a problem that is solvable by a distributed optimization algorithm involves dividing the OCP into subproblems and introducing local copies of all decision variables in each such subproblem [23]. Hence, each individual subproblem involves as many decision variables as the centralized OCP and has a complexity similar to the original problem. As a result, no advantages of distributed control are leveraged.

Therefore, a fully distributed MPC scheme can not be based on the presented centralized prediction model, and it is necessary to adjust the prediction model so that the IBRs' state coupling is no longer global.

III. PROPOSED SOLUTION

We present a procedure to remove state couplings between the IBRs by adjustment of the frequency divider matrix D. In particular, the procedure removes negligible frequency divider entries while preserving the physical interpretability of the frequency values. Afterward, we introduce how the resulting OCP can be partitioned into partly coupled subproblems to be applicable in a practical distributed control setting.

A. FREQUENCY DIVIDER TRIMMING

An entry $D_{(r,i)}$ in the frequency divider matrix gives the contribution of the generation frequency ω_i to an arbitrary bus frequency ω_r. Since the frequency divider calculation is based on the nodal admittance matrix, the magnitude of any $D_{(r,i)}$ depends on the electrical distance between the corresponding two buses. The higher the impedance between them, the lower the magnitude of $D_{(r,i)}$. In large-scale systems, the relative electrical distance of certain generator-bus-combinations might be very high. In such cases, $D_{(r,i)}$ becomes negligibly small, i.e., the impact of a set of distant generators on the dynamics at a particular network node is unimportant. If such entries are approximated to zero, the local frequency only depends on electrically close generators, and some state couplings introduced by (7) are neglected.

We call this procedure *frequency divider trimming*. It consists of two steps: 1) entries of D are set to zero based on specific criteria to obtain the matrix D^neglect; 2) the rows of D^neglect are scaled to obtain the trimmed frequency divider matrix D^trim. In particular, each row is scaled up to a row sum of 1 by applying the following formula

$$D^\mathrm{trim}_{(r,i)} = \frac{D^\mathrm{neglect}_{(r,i)}}{\sum_{r=1}^{(n_b-n_i)} D^\mathrm{neglect}_{(r,i)}}, \quad r \in \mathbb{N}_{[1,(n_b-n_i)]}, \ i \in \mathbb{N}_{[1,n_i]}, \tag{17}$$

where D^neglect and D^trim are $(n_b - n_i) \times n_i$-matrices, while n_b is the number of total buses in the grid and n_i is the number of IBRs.

A particular bus frequency ω_r is calculated by multiplication of the corresponding frequency divider matrix row D_r with ω_G (see (6)), such that the result is a weighted average of all generation frequencies. Hence, the row scaling is

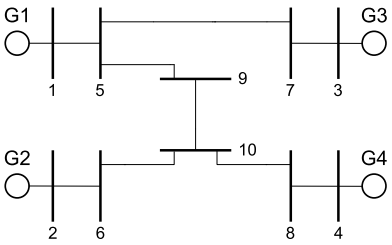

FIGURE 1. Single-line representation of an example grid with four generators.

conducted to ensure that each bus frequency estimated using D^{trim} maintains a total weight of 1, preserving the physical interpretability of the frequency divider after trimming.

We define the procedure for neglecting entries as follows, using two different criteria:

1) Define a threshold th.
2) Define a minimum number of neighbors $\mathcal{N}_{\min}$.
3) Obtain D^{neglect}: If the number of (non-zero) entries in a row D_r remains greater than $\mathcal{N}_{\min}$, set to zero entries $D_{(r,i)} \leq th$ — starting with the smallest entry.

Frequency divider trimming allows adjusting the degree of inter-IBR coupling in the centralized prediction model.

To illustrate the procedure, we consider an exemplary power system shown in Fig. 1 that includes four generators and ten buses.

The generators $G_1, \ldots, G_4$ are connected to buses 1 to 4.

According to (6), ω_{G} consists of the generation frequencies $\omega_1, \ldots, \omega_4$; the remaining bus frequencies are calculated by the frequency divider formula

$$[\omega_5 \quad \omega_6 \quad \omega_7 \quad \omega_8 \quad \omega_9 \quad \omega_{10}]^T = D\,[\omega_1 \quad \omega_2 \quad \omega_3 \quad \omega_4]^T.$$

Evaluating the frequency divider for ω_6, ω_7, and ω_9 yields

$$\begin{aligned}\omega_6 &= 0.15\omega_1 + 0.75\omega_2 + 0.02\omega_3 + 0.08\omega_4\\ \omega_7 &= 0.13\omega_1 + 0.03\omega_2 + 0.82\omega_3 + 0.02\omega_4\\ \omega_9 &= 0.5\omega_1 + 0.22\omega_2 + 0.1\omega_3 + 0.18\omega_4.\end{aligned}$$

The magnitude of frequency divider entries coincides with the electrical distance between buses. For example, the frequency ω_6 is dominated by ω_2 due to the proximity of bus 6 and bus 2. On the contrary, ω_3 contributes very little to ω_6 because of the large electrical distance between bus 3 and bus 6. Similar observations hold for ω_7 and ω_9.

For the frequency divider trimming we choose $th = 5\%$ and $\mathcal{N}_{\min} = 2$. The trimming process yields D^{trim}. Evaluating the trimmed frequency divider for the previously observed frequencies yields

$$\begin{aligned}\omega_6 &\approx 0.153\omega_1 + 0.765\omega_2 + 0\omega_3 + 0.082\omega_4\\ \omega_7 &\approx 0.133\omega_1 + 0.031\omega_2 + 0.837\omega_3 + 0\omega_4\\ \omega_9 &= 0.5\omega_1 + 0.22\omega_2 + 0.1\omega_3 + 0.18\omega_4.\end{aligned}$$

The three frequencies illustrate the effect of the trimming criteria in the trimming process: For ω_6, the influence of ω_3 is neglected, removing the coupling between the two frequencies. The threshold of 5% prevents the neglect of the contribution of ω_4. For ω_7, the influences of both ω_2 and ω_4 are below the threshold and, hence, considered for neglect. However, the minimum number of neighbors $\mathcal{N}_{\min} = 2$ prevents the neglect of both contributions. Only the more minor contribution of ω_4 is neglected. In the case of ω_9, frequency divider trimming does not remove any couplings, as bus 9 has an intermediate electrical distance to all generators.

Summarizing, th and $\mathcal{N}_{\min}$ pose the tuning knobs for methodical frequency divider trimming, yielding a more or less rigorous neglect of entries in D. The threshold criterion assures that negligible frequency couplings are removed during trimming; the minimum number of neighbors criterion provides a baseline for the number of frequency couplings persisting after trimming. Using D^{trim} instead of D, a centralized prediction model can be constructed with fewer state couplings between the different IBRs.

B. PARTITIONING

We demonstrated how to use frequency divider trimming to reduce the state couplings between IBRs in the prediction model, such that state coupling is no longer global. However, each IBR has an individual set of state couplings. Therefore, a resulting centralized OCP might still involve global decision variable coupling in the cost function (10) and the coupling constraints (12a)–(13d), due to the prediction horizon spanning multiple time steps and the decision variable couplings blending with each prediction timestep.

The issue of global decision variable coupling in the centralized OCP, despite the state coupling of the IBRs in the prediction model being only local, motivates further adjustment of the OCP. Inspired by [11], we construct individual partitioned prediction models for each IBR i as

$$\begin{aligned}x^{(i)}(k+1) &= A^{(i)}x^{(i)}(k) + B^{(i)}u^{(i)}(k) + E^{(i)}z^{(i)}(k)\\ y^{(i)}(k) &= C^{(i)}x^{(i)}(k).\end{aligned} \tag{18}$$

Here, $x^{(i)}$ is a stacked vector containing $\{x_i, \{x_j\}_{j\in\mathcal{N}_{j,i}}\}$ where $\mathcal{N}_{j,i}$ is the set of neighbors of IBR i, defined by the remaining state couplings of IBR i after frequency divider trimming. In particular, the neighbors are determined by the IBR frequencies needed to evaluate (6) for IBR i using D^{trim}. Note that frequency divider trimming with a certain $\mathcal{N}_{\min}$ ensures $\left|\mathcal{N}_{j,i}\right| \geq \mathcal{N}_{\min}$ for all IBRs i. Similar to $x^{(i)}$, the vectors $u^{(i)}$ and $z^{(i)}$ are defined as

$$\begin{aligned}u^{(i)} &= \{u_i, \{u_j\}_{j\in\mathcal{N}_{j,i}}\}\\ z^{(i)} &= \{z_i, \{z_j\}_{j\in\mathcal{N}_{j,i}}\}.\end{aligned}$$

In the centralized prediction model, the states of a neighbor j are coupled to different states than the states of IBR i so that the coupling propagates for an increasing number of prediction steps. We set the boundary that each IBR i's

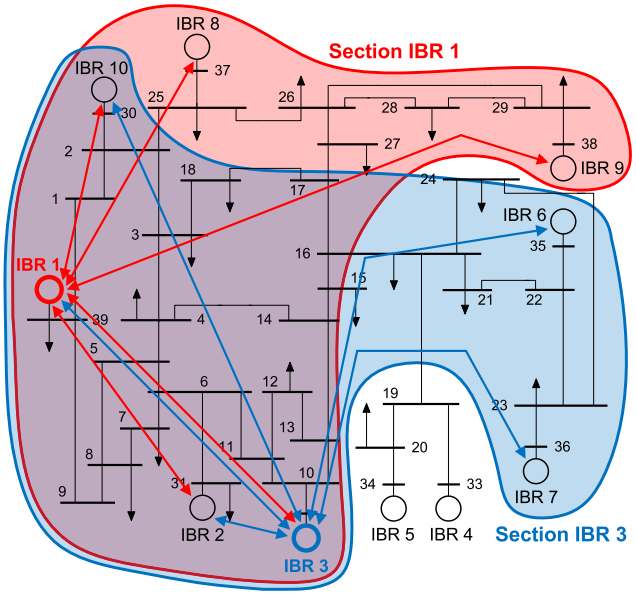

FIGURE 2. Construction of partitioned models for IBRs 1 and 3 in the IEEE 39-bus system.

partitioned prediction model shall only include its initial set of neighbors $\mathcal{N}_{j,i}$ as defined by the frequency divider trimming. Consequently, the prediction model of IBR i includes the state couplings between i and its neighbors j, whereas couplings between any neighbor j and IBRs $\notin \mathcal{N}_{j,i}$ are discarded.

As such, an OCP constructed using the partitioned model of IBR i considers the state information of a limited section in the power system. The trimming criteria th and $\mathcal{N}_{\min}$ define the size of these sections and are tuned so that the sections overlap. Hereby, the overlap of sections ensures that the IBRs' individual OCPs are partly coupled. This means they share a part of their decision variables, particularly the inputs of IBRs considered in multiple partitioned prediction models.

The partitioning approach is illustrated using the example in Fig. 2 with highlighted sections for the IBRs 1 and 3 in the IEEE 39-bus system, which we use for demonstration of the control scheme in Section IV. In this example, the IBRs 1 and 3 consider the state information and coupling with an individual set of 5 neighbors in their prediction model. The IBRs 1, 2, 3, and 10 pose the overlapping part of these sections and are considered in both IBR 1's and 3's prediction models. On the contrary, IBRs 8 and 9 are only part of IBR 1's model, while only IBR 3 considers coupling with IBRs 6 and 7. Neither of the two depicted sections considers the dynamics of the IBRs 4 and 5. Similarly to the shown sections of IBRs 1 and 3, all other IBRs consider individual grid sections, resulting in 10 partly overlapping sections.

The overall procedure for obtaining the partitioned prediction models is summarized in Algorithm 1.

After obtaining the partitioned prediction models, an OCP of the form of (15) can be constructed for each IBR. The resulting individual OCPs for each IBR combine into an overall OCP with a so-called partition-based structure that

Algorithm 1 Construction of Partitioned Prediction Models via Frequency Divider Trimming

Input: Frequency divider matrix D

1) Extract all rows D_g corresponding to grid side buses from D to obtain the matrix D_{G}:

$$D_{\mathrm{G}} := \begin{bmatrix} -D_{g_1}- \\ \vdots \\ -D_{g_{n_i}}- \end{bmatrix}$$

2) Trim D_{G} using the following criteria:
   a) Only entries $\leq th$ are trimmed
   b) Each row has at least $\mathcal{N}_{\min}+1$ entries that are $\neq 0$
   c) All couplings after trimming are bidirectional: If an entry in row g and column i is non-zero after trimming, the entry in the row corresponding to the grid-side bus of i and column corresponding to the IBR of g is also non-zero.

for $i \in \mathcal{N}_i$ **do**

3) Use $D_{\mathrm{G}}^{\mathrm{trim}}$ to construct individual submatrices $D^{(i)}$ for each IBR:
   a) Define the neighborhood of IBR i, $\overline{\mathcal{N}_{j,i}}$: If $D_{\mathrm{G}(i,j)}^{\mathrm{trim}} \neq 0$, IBR j is in the neighborhood of IBR i. By definition, $i \in \overline{\mathcal{N}_{j,i}} = \{i, \mathcal{N}_{j,i}\}$.
   b) Remove all rows of $D_{\mathrm{G}}^{\mathrm{trim}}$ which correspond to buses of IBRs outside of $\overline{\mathcal{N}_{j,i}}$.
   c) Remove all columns $j \notin \overline{\mathcal{N}_{j,i}}$.
   d) To obtain $D^{(i)}$, scale all rows of the remaining matrix, such that each row has a row sum of 1.
4) Construct IBR i's partitioned prediction model (18) analog to the centralized prediction model using $D^{(i)}$, (3), and (7).

end for

involves overlapping of the individual decision variables, as in [24]

$$\begin{aligned} \min_{\{\mathcal{U}_i\}_{i\in\mathcal{N}_i}} \quad & \sum_{i=1}^{n_i} J_i\left(\left\{\mathcal{U}_i, \{\mathcal{U}_j\}_{j\in\mathcal{N}_{j,i}}\right\}\right) \\ \text{s.t.} \quad & \underbrace{\left\{\mathcal{U}_i, \{\mathcal{U}_j\}_{j\in\mathcal{N}_{j,i}}\right\}}_{\mathcal{U}^{(i)}} \in \mathcal{C}_i \quad \forall i \in \mathcal{N}_i. \end{aligned} \tag{19}$$

In this OCP form, each IBR i is optimizing its local cost function J_i subject to its local constraint set $\mathcal{C}_i$. The cost function and the constraints depend on the IBR's local decision variables $\mathcal{U}_i$ and those of its neighboring peers $\mathcal{U}_j$, combining to the partitioned decision vector $\mathcal{U}^{(i)}$. The optimal solution vector $\mathcal{U}^*$ contains all $\mathcal{U}_i^*$ as components [23].

The decision variable coupling of the IBRs' local problems in (19) is identical to the state coupling in their respective prediction models. Thus, the choice of the frequency divider trimming criteria th and $\mathcal{N}_{\min}$ critically influences the coupling structure of the partition-based OCP. In order to indirectly preserve the global coupling nature of the centralized OCP after partitioning, we require the decision variable coupling structure of the partition-based OCP (19)

to be based on a connected graph. We deduce the following requirements:

1) Choose th at least large enough, such that coupling in $D_{\mathrm{G}}^{\mathrm{trim}}$ is not global.
2) Choose $\mathcal{N}_{\min}$ large enough, such that the coupling graph defined by $D_{\mathrm{G}}^{\mathrm{trim}}$ is connected.

C. OPTIMIZATION ALGORITHM

An optimization problem with the structure of (19) can be solved by the algorithms distributed dual decomposition and distributed ADMM. Some variants of these algorithms are tailored to exploit the partitioned structure [23], such as the partition-based relaxed ADMM introduced in [25], which we adopt in this paper. One of the main advantages of these specified algorithms is that each agent/IBR only has access to the decision variables associated with its own problem, while a straightforward application of existing consensus methods would lead to poor scalability and redundancy of shared information [26]. Further, all such algorithms are truly distributed, incorporating a neighbor-to-neighbor communication scheme. The advantages of the partition-based relaxed ADMM include convergence for a clearly defined and wide range of parameter choices. Additionally, the algorithm's convergence is guaranteed under communication losses, which is relevant in a practical implementation. Lastly, ADMM schemes are generally expected to converge faster than dual decomposition algorithms [27].

A detailed pseudo-code description of the partition-based relaxed ADMM is given in [25]. To fully define the algorithm, the parameters $\nu_{\max}$, ρ, and α need to be specified. The maximum number of iterations $\nu_{\max}$ poses the stopping criterion, ρ is an arbitrary penalty parameter as in classical ADMM, and α is a choosable relaxation parameter used to update auxiliary update variables during algorithm execution.

The selected algorithm is designed for bidirectional communication between the executing agents. The communication structure coincides with the inter-IBR coupling structure since coupled agents need to exchange information to reach a consensus on their shared decision variables. As specified in Section III-B, the inter-IBR coupling graph is required to be connected. Thus, we utilize a communication scheme based on a bidirectional and connected communication graph.

D. PROPOSED DISTRIBUTED MPC SCHEME

The proposed distributed MPC scheme consists of local controllers at each IBR collectively performing the partition-based relaxed ADMM algorithm to solve the overall partitioned OCP consisting of the IBRs' local problems with overlapping decision variables. The deployed communication scheme is based on a connected communication graph that directly follows from the IBR couplings remaining after frequency divider trimming. As required in Section III-B, the trimming criteria are chosen so that a connected communication/coupling graph results. This design procedure is independent of the system's operating point since it is based solely on the system's admittance matrix. Online changes in the grid topology impact the admittance matrix. However, in that case, only the values and not the sparsity structure of $D_{\mathrm{G}}^{\mathrm{trim}}$ should be updated since changing the sparsity of $D_{\mathrm{G}}^{\mathrm{trim}}$ would be associated with modifications to the communication scheme. Online addition of communication links is not intended and would be impractical. The removal of available communication links would be wasteful.

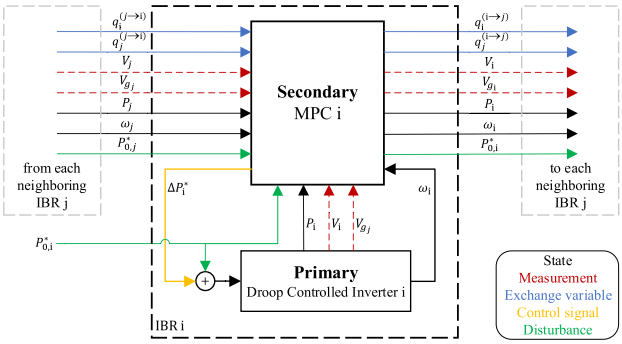

FIGURE 3. Frequency control configuration of each IBR in the distributed MPC scheme.

While keeping the structure of the distributed control problem constant, the OCP has to be initialized in every execution with the current system information. Fig. 3 shows the control configuration of each IBR in the distributed MPC scheme. At each execution call, an IBR i gathers current state information, voltage measurements, and disturbance values associated with itself and each of its neighboring IBRs. After initialization of the OCP, IBR i communicates exchange variables with its neighbors in each iteration of the optimization algorithm.

A flowchart of the distributed MPC scheme is given in Fig. 4. It contains the computation and communication steps of the agents/IBRs as part of the partition-based relaxed ADMM algorithm.

In particular, each IBR i augments its local OCP using auxiliary update variables $p_i^{(j,i)}$ and $p_j^{(j,i)}$. During each iteration of the algorithm, IBR i sends the exchange variables $q_i^{(i\to j)}$ and $q_j^{(i\to j)}$ to its neighbors j while gathering the exchange variables $q_i^{(j\to i)}$ and $q_j^{(j\to i)}$. The auxiliary update variables are then updated at the end of each iteration. Note that slacks are kept local decision variables and are not exchanged during the iterations. After the stopping criterion is reached, each IBR has obtained its optimal partitioned decision variable vector $\mathcal{U}^{(i)^*}$ from which only the first and only the local control input $u_i^*(k \mid k)$ is extracted and used. ν denotes the iteration number.

In case of a short communication loss of an IBR i during the execution of the iterative distributed optimization process, IBR i does not exchange any exchange variables with its neighbors for one or more iterations. In such cases, the algorithm is guaranteed to converge by only updating the auxiliary update variables associated with received exchanged variables. In case of a longer communication

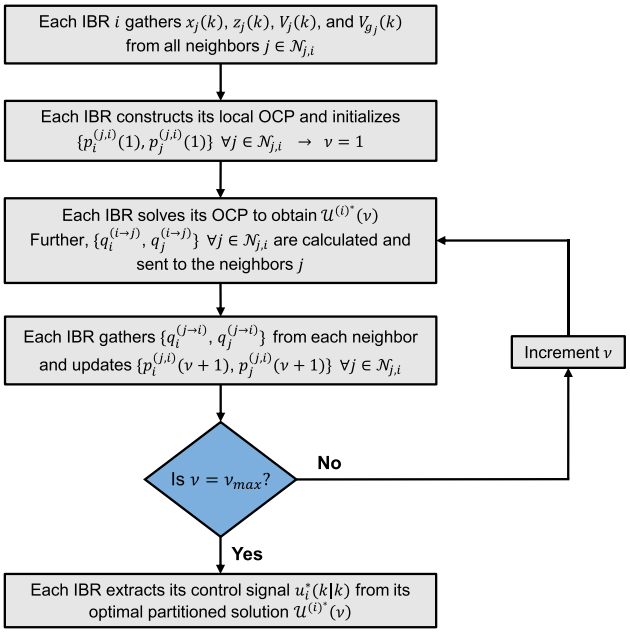

FIGURE 4. Flowchart of the distributed MPC scheme.

loss, IBR i cannot exchange information with its neighbors, including current state and voltage measurement information. Hence, IBR i's OCP is not being updated at a new MPC execution call. In such cases, the distributed MPC scheme maintains operation by each IBR using the latest available information from its neighbors for its current local OCP.

IV. EVALUATION

The proposed distributed MPC for secondary frequency control is evaluated in numerical time-domain simulations of the IEEE 39-bus system and an extended CIGRE medium voltage power system, carried out in MATLAB/Simulink. The distributed control scheme is initially compared to the centralized version of the controller presented in [19]. Additionally, scenarios of communication loss are considered to evaluate the robustness, and the influence of different tuning parameters is discussed.

A. SYSTEM DESCRIPTION IEEE 39-BUS SYSTEM

The chosen system for implementing the distributed MPC is the IEEE 39-bus system, a model of the high-voltage transmission system of the New England area. The power system model represents a meshed network consisting of 10 generators, 19 loads, and 46 lines. In the original model, all generation is synchronous. To obtain an inverter-based power system, we replace all the synchronous generation with IBRs. The IBRs all are operated as voltage sources in the grid-forming control mode. As such they establish a voltage and frequency independently without relying on an external grid. Furthermore, they provide a virtual inertia and primary frequency response via the well-known droop control [1]. Inner control loops and LCL filter dynamics of each IBR are modeled in the simulation as described in [19].

The nominal system voltage is $V_\mathrm{n} = 345\,\mathrm{kV}$. Like the original synchronous generators, we operate the IBRs in conjunction with step-up transformers, such that the nominal voltage of buses 30–38 is 22 kV. The system is operated at a nominal frequency of $f_\mathrm{n} = 50\,\mathrm{Hz}$, and each IBR is rated with the base apparent power of 100 MVA.

Active power and voltage set-points are assumed to be determined in steady-state by a higher-level control instance that optimizes the power flow. The secondary frequency control is implemented by the distributed MPC, which adjusts the steady-state active power set-points by ΔP_i^*.

B. FREQUENCY DIVIDER TRIMMING SENSITIVITY ANALYSIS

A quantitative study was performed to analyze the impact of frequency divider trimming and its criteria threshold th and minimum number of neighbors $\mathcal{N}_\mathrm{min}$ on the accuracy of the prediction model. We have considered 25 trimming cases with th ranging from 2.5% to 10% and $\mathcal{N}_\mathrm{min}$ ranging from 1 to 5. For these 25 cases, the proposed frequency divider trimming procedure was applied, and the corresponding trimmed frequency divider matrices D^trim were stored. The resulting coupling/communication graphs are highly meshed for low values of th and high values of $\mathcal{N}_\mathrm{min}$. The communication graphs become increasingly sparse when the threshold is increased and the minimum number of neighbors is decreased. In summary, the trimming removes many inter-IBR couplings when th is high and $\mathcal{N}_\mathrm{min}$ is low.

To quantitatively study the impact of trimming, a quasi Monte Carlo simulation approach was conducted using Halton sequences. Through Halton sequences, randomized load steps at buses 12, 15, 16, 23, 24, and 27 were generated with a magnitude between defined limits $P_\mathrm{step,min}$ and $P_\mathrm{step,max}$. The sum of all worst case load steps was 525 MW. Using Halton sequences allows to uniformly cover the load step scenarios without bias. A total of 70 simulation runs were performed and the normalized root mean square error (RMSE) of the frequency estimation by each trimmed frequency divider matrix was calculated by comparing it with the phasor measurement unit (PMU) frequency at each IBR's grid side bus. Additionally, the RMSE of the non-trimmed frequency divider was calculated. For easy visualization, the RMSE of each trimming case was scaled with the RMSE of the non-trimmed frequency divider.

$$RMSE_\mathrm{trim,scaled} = \frac{RMSE_{D^\mathrm{trim}}}{RMSE_D}$$

To study the overall impact of the various trimming cases, the scaled $RMSE_\mathrm{trim,scaled}$ averaged over all grid side buses was investigated. Fig. 5 shows the scaled RMSE for all variations of th and $\mathcal{N}_\mathrm{min}$. It can be observed that the scaled RMSE for trimming cases with a given $\mathcal{N}_\mathrm{min}$ approaches unity when th is decreased. Vice versa, for a given th, increasing $\mathcal{N}_\mathrm{min}$ also reduces the scaled RMSE towards 1. Cases with a scaled RMSE close to 1 involve a high number

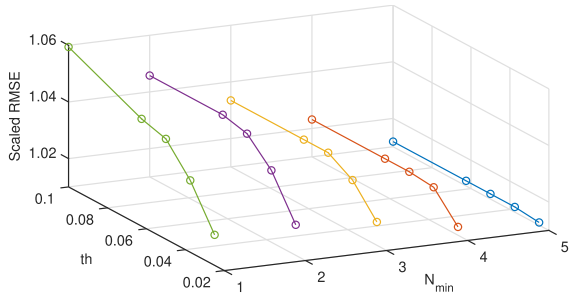

FIGURE 5. Scaled RMSE over all buses as threshold and minimum number of neighbors are varied in frequency divider trimming.

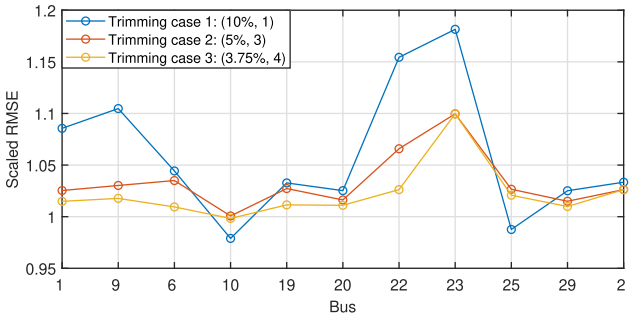

FIGURE 6. Scaled RMSE at all IBR grid side buses in the IEEE-39-bus system.

of couplings, while in cases with a high RMSE, the coupling scheme is less complex. Thus, the selection of th and $\mathcal{N}_{\min}$ is a tradeoff between accuracy and the number of IBR couplings.

For the distributed MPC in the IEEE 39-bus system, the choice of the frequency divider trimming criteria was made according to the requirements defined in Section III-B, i.e., such that a connected coupling graph results while considering the insights given in Fig. 5. The proposed trimming criteria are $th = 5\,\%$ and $\mathcal{N}_{\min} = 3$. The accuracy of the proposed trimming case is approximately within $3\,\%$ of the non-trimmed frequency divider.

To study the accuracy using D^{trim} at each IBR's grid side bus individually, the scaled RMSE was evaluated at each of these buses. We considered three trimming cases: case 1 with $th = 10\,\%$ and $\mathcal{N}_{\min} = 1$ resulting in a disconnected coupling graph, the selected case 2 with $th = 5\,\%$ and $\mathcal{N}_{\min} = 3$, and case 3 with $th = 3.75\,\%$ and $\mathcal{N}_{\min} = 4$ with a complex coupling structure. Fig. 6 shows the scaled RMSE at each grid side bus for the three trimming cases. As observed, the RMSE is worst for case 1, whereas cases 2 and 3 have a similar RMSE for most buses. This further justifies the proposed trimming criteria selection.

Reducing the threshold and increasing the minimum number of neighbors further does not lead to a significant RMSE reduction, while the number of communication links increases, thereby losing practical significance.

To further analyze the effect of frequency divider trimming, time domain simulations were performed, in which the frequency measurements obtained from a PMU and the frequency estimation of the non-trimmed frequency divider are evaluated along with the estimations using trimming cases

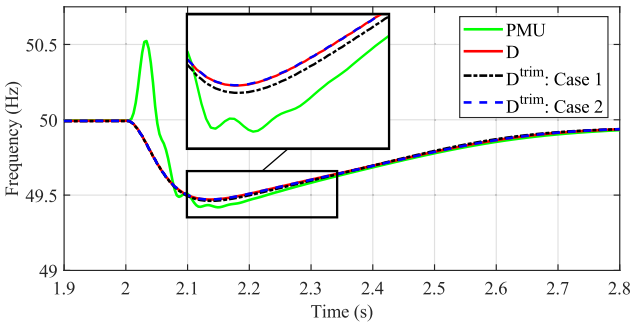

FIGURE 7. Comparison of frequency estimations at bus 10 in the IEEE 39-bus system after a load step.

1 and 2. These simulations involve a load step at $t = 2\,\text{s}$. The time domain results at bus 10 are shown in Fig. 7. It is observed that both case 1 and 2 are in close agreement with the non-trimmed frequency divider D. However, as shown in the zoomed scope, the frequency estimation of trimming case 2 is closer to D than trimming case 1. These results are consistent at each grid side bus.

C. CONTROLLER DESIGN

Designing the distributed MPC scheme involves specifying the inter-IBR communication/coupling structure resulting from frequency divider trimming and choosing the controller parameters.

The frequency divider trimming criteria were specified according to the sensitivity analysis in Section IV-B as $th = 5\%$ and $\mathcal{N}_{\min} = 3$. The resulting partitioning defines the communication scheme of the distributed MPC, as depicted in Fig. 8. Subsequently, the parameters of the distributed MPC scheme were specified as shown in Table 1. The parameters related to the partition-based relaxed ADMM ρ and α were tuned in a try-and-error procedure for fast convergence of the algorithm within the simulation setup described in Subsection IV-E. Afterward, $\nu_{\max}$ was specified as a value guaranteeing sufficient solution accuracy.

A warm start strategy was implemented in the MPC scheme, meaning that all IBRs store the auxiliary update and exchange variables as well as their solutions at the end of each MPC execution to use them as initial values in the next algorithm execution. It was observed that the implementation of a warm start speeds up the convergence of the algorithm.

The MPC tuning parameters are Q, R, S, and the equally specified horizons $H_{\text{p}} = H_{\text{u}}$. Q is orders of magnitude higher than R and S, since the numerical values of $y(k+j \mid k)$ are orders of magnitude smaller than $u(k+j \mid k)$. Additionally, the value of Q is weighted much higher than R and S to ensure that frequency regulation is the primary control objective of the proposed OCP. The value of R was tuned to achieve a damped control response. A small value of S was chosen to incentivize the MPC to optimize for equal power sharing in steady-state while not interfering with the frequency regulation objective. The horizons $H_{\text{p}} = H_{\text{u}}$ were chosen in an iterative tuning procedure starting from an initial value of 3. The chosen value of 4 achieves a balanced tradeoff

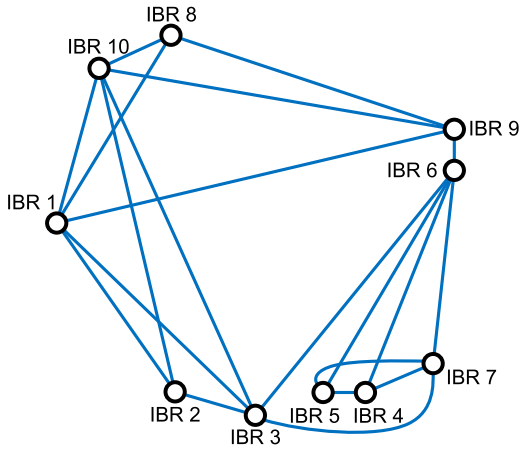

FIGURE 8. Communication/coupling graph of the distributed MPC in the IEEE 39-bus system.

TABLE 1. Parameters of the distributed MPC in the IEEE 39-bus system.

Parameter	Description	Value
T_s	Sampling Time	100 ms
H_p	Prediction Horizon	4
H_u	Control Horizon	4
Q	Weight on Output Error	$2 \cdot 10^7$
R	Weight on Input Changes	10^{-7}
S	Weight on Absolute Inputs	10^{-9}
ρ_1, ρ_2, ρ_3	Weights on Slack Variables	$10^{10}, 10^{10}, 10^4$
ν_max	max. Number of Iterations	10
ρ	Penalty Parameter	$5 \cdot 10^{-8}$
α	Relaxation Parameter	0.8
f_max	max. Frequency	51.5 Hz
f_min	min. Frequency	47.5 Hz
Δf_max	max. RoCoF	3 Hz/s
Δf_min	min. RoCoF	−3 Hz/s
$P_{i,\mathrm{max}}$	max. Active Power	100 MW
$P_{i,\mathrm{min}}$	min. Active Power	0 MW
$u_{i,\mathrm{max}}$	max. Input	$100\,\mathrm{MW} - P^*_{0,i}$
$u_{i,\mathrm{min}}$	min. Input	$-P^*_{0,i}$
$\tau_{i,\mathrm{p}}$	Droop Filter Time Constant	100 ms
$m_{i,\mathrm{p}}$	Droop Gain	0.03 pu
$P_{0,i}$	Pre-Event P Setpoint	60 MW

between control performance and algorithm convergence speed. During the tuning process, we observed that larger horizons yielded better overall performance of the distributed MPC in the simulations, while the algorithm converged within fewer iterations for smaller horizons.

D. COMMUNICATION DELAYS

Classical secondary frequency control has been assigned a time range of 15 s to 15 min after an event, e.g., [28], and correspondingly communication delays of 250 ms or more have been considered acceptable [29] for monitoring frequency stability. However, the novel method proposed in this paper operates at a faster timescale and, in particular, the MPC samples at 100 ms. For this application, typical existing IP-based networks, e.g., using PMUs, will likely not fulfill the required communication speed. For example, measurements of a real communication network in [30] indicate several hundreds of milliseconds of communication delay (depending on the distance). Instead, a dedicated, fast, and deterministic communication is assumed for the application of the novel control method proposed in this paper, e.g. using dedicated fiber optics, leading to presumably negligible communication delays of a few milliseconds/100 km.

TABLE 2. Load step events.

Time	Location	Value	Time	Location	Value
5 s	Bus 3	+70 MW	10 s	Bus 3	−70 MW
	Bus 8	+30 MW		Bus 8	−30 MW
	Bus 15	+70 MW		Bus 15	−70 MW
	Bus 20	+65 MW		Bus 20	−65 MW
	Bus 24	+45 MW		Bus 24	−45 MW
	Bus 25	+55 MW		Bus 25	−55 MW
	Total	+335 MW		Total	−335 MW

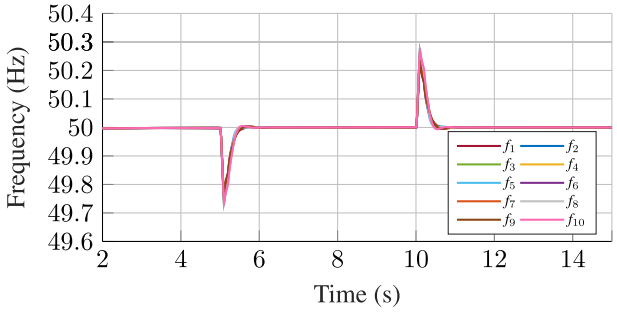

(a) Frequencies

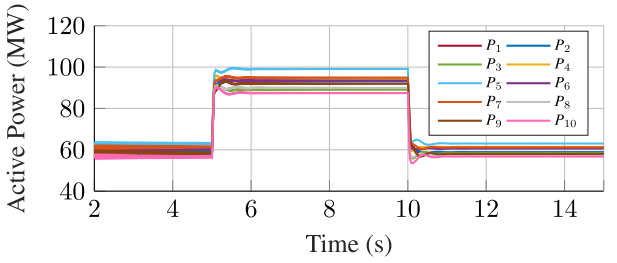

(b) Active powers

FIGURE 9. IBR frequencies and active power outputs controlled by the distributed MPC in the IEEE 39-bus system.

E. SIMULATION RESULTS IEEE 39-BUS SYSTEM

The performance of the control response is validated for a step increase and subsequent decrease of the system load. The initial system load sums up to $P_\mathrm{load,total} = 600$ MW. At $t = 5$ s, the load is increased at several buses, adding up to a total step of 335 MW. The additional load is removed at $t = 10$ s. A detailed summary of the load changes is given by Table 2. Fig. 9 shows each IBR's frequency and active power output during a simulation run while the secondary distributed MPC is active.

It is observed that the active powers are quickly stabilized, and the frequency is recovered into a ±0.01 Hz band around 50 Hz within 510 ms in both transients.

To properly evaluate the distributed MPC, it is compared to the centralized version of the controller in [19] and a centralized PI controller. Since the centralized MPC

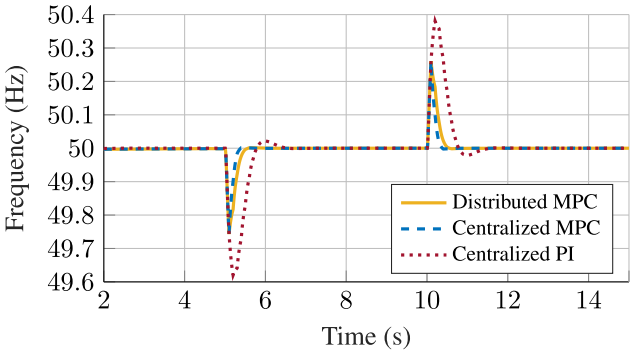

FIGURE 10. Average of the IBR frequencies in the IEEE 39-bus system for the proposed distributed MPC, the centralized MPC, and a centralized PI controller.

TABLE 3. Performance measures in the IEEE 39 bus system.

Measure	Distr. MPC	Centr. MPC	Centr. PI
$e_{\mathrm{ss,max}}$	$1.9 \cdot 10^{-4}$ Hz	$2.2 \cdot 10^{-4}$ Hz	$6.4 \cdot 10^{-4}$ Hz
ISE_{max}	0.1025	0.0725	0.3206
$t_{\mathrm{rec,max}}$	0.509 s	0.441 s	1.270 s

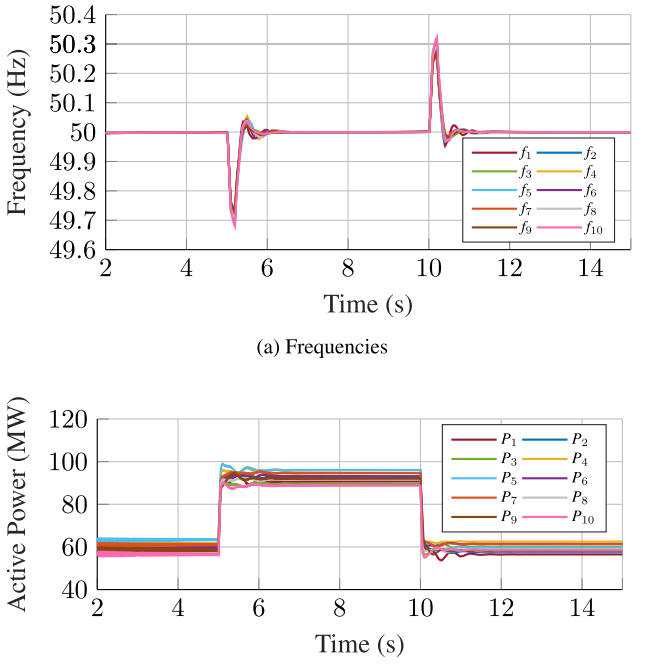

(a) Frequencies

(b) Active powers

FIGURE 11. IBR frequencies and active power outputs controlled by the distributed MPC in the IEEE 39-bus system, while each MPC execution call is terminated after one iteration.

uses the same prediction model as the distributed MPC but without frequency divider trimming, it serves as an upper bound for control performance. The PI controller serves as a performance benchmark. Fig. 10 shows the average of the IBR frequencies during a simulation run for all three considered controllers. The control response of the distributed MPC is observed to be similar to the centralized MPC and significantly faster than the centralized PI controller. The frequency recovery time of the distributed MPC is slightly increased by approximately 70 ms. The frequency nadirs are almost identical for the centralized and the distributed MPC, in particular, 49.725 Hz (distributed) compared to 49.724 Hz for the positive load step. The nadirs for the negative load step are 50.278 Hz (distributed) and 50.280 Hz, respectively. In contrast, the nadirs of the centralized PI controller deviate an additional 120 mHz from the nominal frequency for each load step. Table 3 shows a quantitative comparison between the controllers in terms of performance measures, i.e., the steady-state frequency error $e_{\mathrm{ss,max}}$, the integral squared error ISE_{max}, and the frequency recovery time $t_{\mathrm{rec,max}}$. The index max denotes that the worst-case value among all IBRs is observed. All controllers achieve a steady state error in the order of 10^{-4} Hz.

Overall, the performance of distributed and centralized MPC remains comparable, which is emphasized by the similar values of the *ISE*, a measure of overall performance. Thus, the distributed MPC proves advantageous since it can leverage benefits of distributed control, such as scalability, avoiding a single point of failure, and limited requirements on communication infrastructure by requiring only information exchange within a defined neighborhood. When comparing distributed MPC and centralized MPC, we note that there is, in general, no guarantee that satisfying the constraints of the partitioned OCP implies that the constraints for the more accurate centralized OCP are satisfied. However, the principal difference between the models is the estimation of the frequency f_g at the each IBR's grid side bus. When approaching steady state, all IBR frequencies approach the nominal frequency, and the error introduced by frequency divider trimming with respect to the frequency amplitude vanishes, such that the constraints of the centralized OCP are met with negligible error.

As described in Section III-C, the IBRs in the distributed optimization algorithm are iteratively exchanging information about their decision variables, i.e., the control inputs over the control horizon $\mathcal{U}^*(k)$, with other IBRs within their predetermined control sections. In Fig. 9, the distributed optimization was stopped after $\nu_{\mathrm{max}} = 10$ iterations in each algorithm call, a value that guaranteed convergence close to the optimal solution. The optimization algorithm can be terminated earlier to reduce the vulnerability to communication delays and information loss as well as to decrease the computational burden. Fig. 11 presents the simulation results when the optimization is terminated after only $\nu_{\mathrm{max}} = 1$ iteration.

It can be seen that the control performance does not critically decline. In this case, the frequency has a slight overshoot, and the active power response has a marginally longer transient, such that the system reaches steady-state (± 0.01 Hz) after 1040 ms. We conclude that the requirements on the computation and communication systems can be significantly reduced for an acceptable cost of performance.

In Fig. 12 the communication with IBR 4 is lost from $t = 7.5$ s until $t = 12.5$ s. A total loss of communication

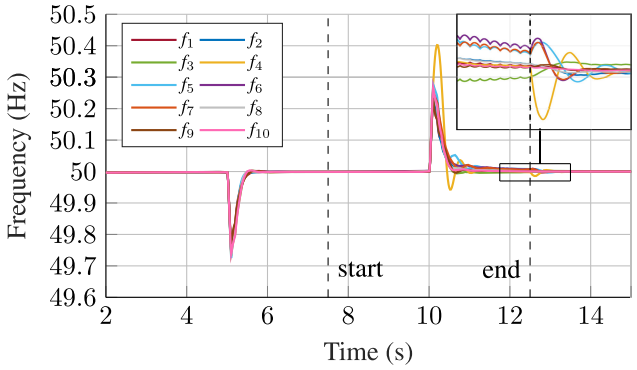

(a) Frequencies

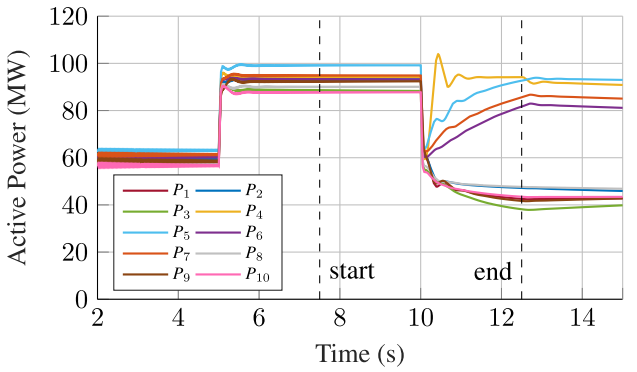

(b) Active powers

FIGURE 12. IBR frequencies and active power outputs controlled by the distributed MPC in the IEEE 39-bus system during a communication loss of IBR 4 (7.5 s–12.5 s).

over the span of multiple sampling times means that IBR 4 is neither sending nor receiving any information to/from its neighboring IBRs. According to Fig. 3, this results in missing updates of state variables, voltage measurements, and algorithm exchange variables. As specified in Section III-D, the distributed MPC continues execution using the latest available information. The maximum number of iterations of the optimization is again set to 10.

During steady-state, the loss of communication has no impact on the power system. Due to the warm start strategy, the optimization is initialized with the variables and solution from the previous time step. Thus, no deviation due to communication loss is observed. The communication is restored 2.5 s after the load step at $t = 10$ s. It can be observed that the frequency recovers with a stable response. In particular, steady-state (± 0.01 Hz) is reached within 1180 ms. When the communication is restored, IBR 4 reattains access to state and voltage information updates. As a result, the steady-state frequency error tightens, as emphasized in the zoomed scope. Due to the communication loss, the frequency at IBR 4 shows an increased nadir of 50.402 Hz and overshoots noticeably. The active power sharing is more uneven compared to the previous cases, and the power output is subject to a larger overshoot. However, the spread in power outputs slowly reduces after $t = 12.5$ s due to the penalty on absolute inputs. We note that the system remains stable also for a longer, simultaneous communication loss of two IBRs until $t = 15$ s, however, at the cost of larger transient responses in the frequency and active power.

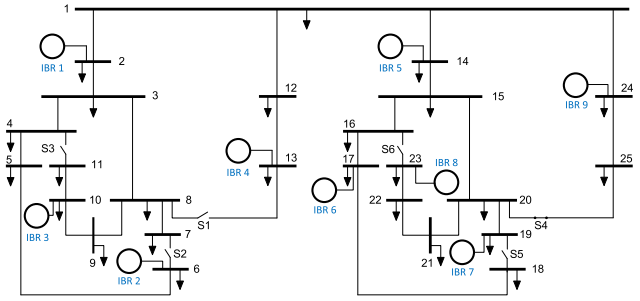

FIGURE 13. Single-line diagram of the extended CIGRE MV system.

In general, the distributed MPC can handle a loss of communication of some IBRs. If too many IBRs lose communication simultaneously for an extended amount of time, fallback strategies should be implemented, such as reverting to a decentralized secondary control or turning the secondary control off and relying only on the primary control. However, the design of such fallback strategies is outside the scope of this paper.

F. SYSTEM DESCRIPTION EXTENDED CIGRE MV SYSTEM

The second chosen system for implementation and simulation of the proposed distributed MPC is an extension of the medium voltage distribution network benchmark introduced by CIGRE in [31]. The extended CIGRE MV system in this paper is modeled as a parallel connection of two MV systems in the European configuration to a common bus. The extended CIGRE MV system has a total of 25 buses. Nine grid-forming IBRs, which serve as the only generation units, were placed evenly throughout the grid. A single-line diagram of the system is shown in Fig. 13. The two subsystems are not identical due to the different placement of the IBRs and different switch positions. As depicted in Fig. 13, switch S4 is closed to form a ring connection in the right subsystem while the other switches are open, so that the remaining grid has a mostly radial structure. The IBRs each have a rated power of 5 MW with an equal time constant of 100 ms of the first order active power filter. The system has a nominal voltage of 20 kV. Further system parameters are obtained from [31].

G. SIMULATION RESULTS EXTENDED CIGRE MV SYSTEM

Overall, the controller design of the distributed MPC was conducted similarly to the IEEE 39-bus system, with the difference that prediction model and OCP were set up using a per-unit representation of all variables. The frequency divider trimming criteria were chosen as $th = 6.25\,\%$ and $\mathcal{N}_{\min} = 1$, according to the guidelines provided in Sections III-B and IV-B. The resulting communication/coupling graph of the distributed MPC is displayed in Fig. 14.

A summary of the selected control parameters is given in Table 4. The sampling time was reduced from 100 ms to 25 ms to account for the faster frequency dynamics

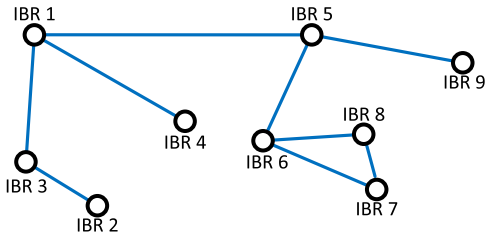

FIGURE 14. Communication/coupling graph of the distributed MPC in the extended CIGRE MV system.

TABLE 4. Parameters of the distributed MPC in the extended CIGRE MV system.

Parameter	Description	Value
T_s	Sampling Time	25 ms
H_p	Prediction Horizon	4
H_u	Control Horizon	4
Q	Weight on Output Error	200
R	Weight on Input Changes	0.5
S	Weight on Absolute Inputs	10^{-4}
ρ_1, ρ_2, ρ_3	Weight on Slack Variables	$10^4, 10^4, 10^4$
ν_max	max. Number of Iterations	6
ρ	Penalty Parameter	0.11
α	Relaxation Parameter	0.8
$\tau_{i,\mathrm{p}}$	Droop Filter Time Constant	100 ms
$m_{i,\mathrm{p}}$	Droop Gain	0.03 pu

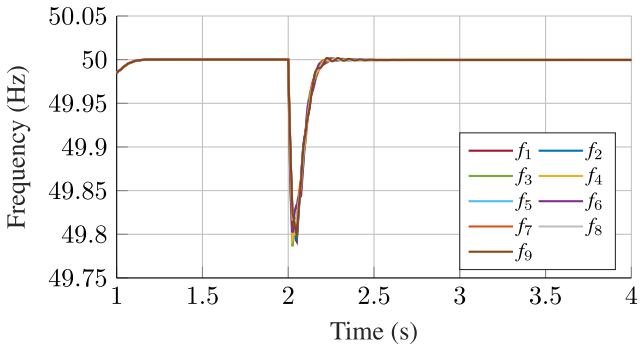

FIGURE 15. Controlled IBR frequencies in the extended CIGRE MV system using the distributed MPC.

due to shorter line lengths. The weights Q, R, and S, as well as the penalty parameter ρ, have different orders of magnitude compared to the IEEE 39-bus system case in Table 1, since the per-unit method was used. Again, a warm start was implemented to accelerate the convergence of the optimization algorithm.

The considered simulation scenario includes a load step increase at various buses in the system at $t = 2\,\mathrm{s}$, with a total of 9 MW. The initial system load is 9.43 MW. Fig. 15 shows the corresponding IBR frequencies controlled by the distributed MPC.

As noted in Table 4, the control scheme could achieve convergence to sufficient accuracy after a maximum of $\nu_\mathrm{max} = 6$ iterations in every execution call. The IBR frequencies recover to a ± 0.01 Hz band around 50 Hz within 190 ms after the load step. The maximum frequency nadir is 49.786 Hz. A quantitative performance comparison with the centralized version of the MPC and a centralized PI controller is given in Table 5.

TABLE 5. Performance measures in the extended CIGRE benchmark system.

Measure	Distr. MPC	Centr. MPC	Centr. PI
$e_{\mathrm{ss,max}}$	$3.8 \cdot 10^{-4}$ Hz	$3.8 \cdot 10^{-4}$ Hz	$6.1 \cdot 10^{-6}$ Hz
$\lvert\Delta f\rvert_\mathrm{max}$	0.2137 Hz	0.2137 Hz	0.2495 Hz
ISE_max	0.00261	0.00267	0.00998
$t_{\mathrm{rec,max}}$	0.190 s	0.195 s	0.835 s

The distributed MPC performs almost identically to the centralized MPC, which uses the same control parameters. The integral squared error and the recovery time of the MPCs are by a factor of four smaller than for the centralized PI controller. At the same time, the MPCs achieve a 35 mHz smaller maximum frequency deviation. The steady-state error of the MPCs is again in the order of 10^{-4} Hz.

To evaluate the computational effort of the distributed MPC, a runtime analysis of the described simulation run was conducted, using a PC with Intel Core i5-10210U CPU and 16 GB of RAM. During the simulation run, the distributed MPC was executed 160 times. The total required execution time associated with construction of the IBRs' local OCPs was 0.503 s, while performing the partition-based relaxed ADMM algorithm required a total of 2.497 s. The resulting computation time per execution of the distributed MPC was 18.9 ms. If considering a simultaneous parallel execution by each IBR's computation unit, the average computation time per execution per IBR would be $t_{exec,i} = 2.1\,\mathrm{ms}$. These results show that the computation of the optimal control signals can be performed in a fraction of the MPC sampling time $T_s = 25\,\mathrm{ms}$. The remaining time difference of 22.9 ms would be available for communication delays, which were not considered in the implementation in MATLAB/Simulink. The delay, which a real dedicated communication scheme would introduce, might be greater than the available time difference between T_s and $t_{exec,i}$, however, the computation time using optimized code running on specialized control hardware is likely to be lower than in the presented runtime analysis.

Similarly to the IEEE 39-bus system, the robustness of the distributed MPC is evaluated by investigating the effects of two scenarios: 1) early termination of each MPC execution call after one iteration and 2) communication loss of an arbitrary IBR. Fig. 16 shows the IBR frequencies in the two considered scenarios, and for the unimpaired distributed MPC. Stable frequency responses are observed in all scenarios. The control performance under early termination is comparable to the base case without communication loss, with a 13% increase in maximum frequency recovery time and an 11% larger maximum frequency nadir. During the communication loss of IBR 6 between 1.5 s and 3.5 s, no effect is visible in steady state. However, the IBR frequencies recover slower after the load step than in the base case without communication loss. After the communication

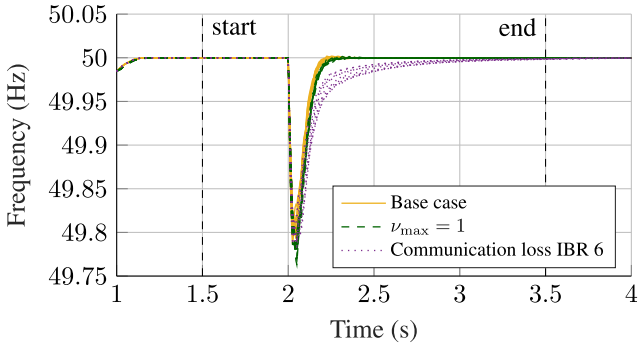

FIGURE 16. Controlled IBR frequencies in the extended CIGRE MV system using the distributed MPC for different scenarios.

is restored at 3.5 s, the small remaining frequency error vanishes. In summary, the observed results are consistent with the results of the IEEE 39-bus system.

V. CONCLUSION

This paper presents a distributed MPC scheme for secondary frequency control of inverter-based power systems. The distributed MPC is based on the partition-based relaxed ADMM, which solves a global optimization problem that is partitioned into local subproblems with overlapping decision variables. The proposed control architecture consists of local controllers at each IBR that exchange local measurement information and temporary exchange variables among a defined set of neighbors. We propose the method of *frequency divider trimming* for generating an approximation of the frequency divider by introducing sparsity into the frequency divider matrix D. The method enables the creation of partitioned submodels by splitting the centralized frequency prediction model into overlapping sections while preserving the physical interpretability of the first-principles modeling equations. In simulations, it was shown that:

1) Transient frequency estimations using a trimmed frequency divider matrix D^{trim} are in close agreement with the full frequency divider if the trimming criteria are selected accordingly. In the performed sensitivity analysis, the errors are in the range of $< 3\,\%$.
2) The proposed distributed MPC scheme achieves a control performance comparable to the centralized MPC in [19] based on the same prediction model. In the two considered test systems, the frequency recovery time of the distributed MPC after a load step is 0 %–16 % longer, while the occurring frequency nadir is identical to the centralized MPC.
3) The distributed MPC leverages two advantages of distributed control. In particular, it is scalable, as the complexity of each IBR's local OCP does not scale with the number of IBRs in the grid. Further, the required communication scheme only involves neighbor-to-neighbor communication.
4) By terminating the algorithm after one iteration, the computational burden and requirements on communication systems can be significantly reduced at an acceptable expense of additional frequency recovery time, i.e., 13%–104% in the performed simulations.
5) The distributed MPC scheme is robust against communication losses spanning multiple controller sampling times.

ACKNOWLEDGMENT

At the time of writing, Ilka Jahn was with the Institute for Automation of Complex Power Systems, RWTH Aachen University.

REFERENCES

[1] R. Rosso, X. Wang, M. Liserre, X. Lu, and S. Engelken, "Grid-forming converters: Control approaches, grid-synchronization, and future trends—A review," *IEEE Open J. Ind. Appl.*, vol. 2, pp. 93–109, 2021.
[2] F. Milano, F. Dörfler, G. Hug, D. J. Hill, and G. Verbic, "Foundations and challenges of low-inertia systems (invited paper)," in *Proc. Power Syst. Comput. Conf. (PSCC)*, Jun. 2018, pp. 1–25.
[3] K. Liu, L. Yang, T. Liu, and D. J. Hill, "Distributed model predictive frequency control of inverter-based networked microgrids," *IEEE Trans. Energy Convers.*, vol. 36, no. 4, pp. 2623–2633, Dec. 2021.
[4] Z. Guo, S. Li, and Y. Zheng, "Feedback linearization based distributed model predictive control for secondary control of islanded microgrid," *Asian J. Control*, vol. 22, no. 1, pp. 460–473, Jan. 2020.
[5] J. W. Simpson-Porco, Q. Shafiee, F. Dörfler, J. C. Vasquez, J. M. Guerrero, and F. Bullo, "Secondary frequency and voltage control of islanded microgrids via distributed averaging," *IEEE Trans. Ind. Electron.*, vol. 62, no. 11, pp. 7025–7038, Nov. 2015.
[6] A. N. Venkat, J. B. Rawlings, and S. J. Wright, "Stability and optimality of distributed model predictive control," in *Proc. 44th IEEE Conf. Decis. Control*, Dec. 2005, pp. 6680–6685.
[7] L. Yang, T. Liu, and D. J. Hill, "Distributed MPC-based frequency control for multi-area power systems with energy storage," *Electr. Power Syst. Res.*, vol. 190, Jan. 2021, Art. no. 106642.
[8] A. J. Babqi, "A novel model predictive control for stability improvement of small scaled zero-inertia multiple DGs micro-grid," *Periodica Polytechnica Electr. Eng. Comput. Sci.*, vol. 66, no. 2, pp. 163–173, May 2022.
[9] F. Garcia-Torres, A. Zafra-Cabeza, C. Silva, S. Grieu, T. Darure, and A. Estanqueiro, "Model predictive control for microgrid functionalities: Review and future challenges," *Energies*, vol. 14, no. 5, p. 1296, Feb. 2021.
[10] K. Liu, T. Liu, Z. Tang, and D. J. Hill, "Distributed MPC-based frequency control in networked microgrids with voltage constraints," *IEEE Trans. Smart Grid*, vol. 10, no. 6, pp. 6343–6354, Nov. 2019.
[11] A. N. Venkat, I. A. Hiskens, J. B. Rawlings, and S. J. Wright, "Distributed MPC strategies with application to power system automatic generation control," *IEEE Trans. Control Syst. Technol.*, vol. 16, no. 6, pp. 1192–1206, Nov. 2008.
[12] X. Liu, Y. Zhang, and K. Y. Lee, "Coordinated distributed MPC for load frequency control of power system with wind farms," *IEEE Trans. Ind. Electron.*, vol. 64, no. 6, pp. 5140–5150, Jun. 2017.
[13] F. Milan and Á. Ortega, "Frequency divider," *IEEE Trans. Power Syst.*, vol. 32, no. 2, pp. 1493–1501, Mar. 2017.
[14] Á. Ortega, A. Musa, A. Monti, and F. Milano, "Hardware-in-the-loop validation of the frequency divider formula," in *Proc. IEEE Power Energy Soc. Gen. Meeting (PESGM)*, Aug. 2018, pp. 1–5.
[15] B. Tan, J. Zhao, N. Duan, D. A. Maldonado, Y. Zhang, H. Zhang, and M. Anitescu, "Distributed frequency divider for power system bus frequency online estimation considering virtual inertia from DFIGs," *IEEE J. Emerg. Sel. Topics Circuits Syst.*, vol. 12, no. 1, pp. 161–171, Mar. 2022.
[16] J. Zhao, L. Mili, and F. Milano, "Robust frequency divider for power system online monitoring and control," *IEEE Trans. Power Syst.*, vol. 33, no. 4, pp. 4414–4423, Jul. 2018.
[17] T. Heins, P. Chanfreut, S. K. Gurumurthy, P. Srivastava, A. Monti, and A. M. Annaswamy, "Distributed frequency divider-based model predictive control for frequency control of multi-area power systems," in *Proc. IEEE Int. Conf. Commun., Control, Comput. Technol. Smart Grids (SmartGridComm)*, Oct. 2023, pp. 1–7.
[18] A. M. Ersdal, L. Imsland, and K. Uhlen, "Model predictive load-frequency control," *IEEE Trans. Power Syst.*, vol. 31, no. 1, pp. 777–785, Jan. 2016.

[19] T. Heins, M. Joševski, S. K. Gurumurthy, and A. Monti, "Centralized model predictive control for transient frequency control in islanded inverter-based microgrids," *IEEE Trans. Power Syst.*, vol. 38, no. 3, pp. 2641–2652, May 2023.
[20] S. D'Arco and J. A. Suul, "Equivalence of virtual synchronous machines and frequency-droops for converter-based MicroGrids," *IEEE Trans. Smart Grid*, vol. 5, no. 1, pp. 394–395, Jan. 2014.
[21] J. Liu, Y. Miura, and T. Ise, "Comparison of dynamic characteristics between virtual synchronous generator and droop control in inverter-based distributed generators," *IEEE Trans. Power Electron.*, vol. 31, no. 5, pp. 3600–3611, May 2016.
[22] J. M. Maciejowski, *Predictive Control With Constraints*. Upper Saddle River, NJ, USA: Prentice-Hall, 2001.
[23] G. Notarstefano, I. Notarnicola, and A. Camisa, "Distributed optimization for smart cyber-physical networks," *Found. Trends Syst. Control*, vol. 7, no. 3, pp. 253–383, 2020.
[24] T. Erseghe, "A distributed and scalable processing method based upon ADMM," *IEEE Signal Process. Lett.*, vol. 19, no. 9, pp. 563–566, Sep. 2012.
[25] N. Bastianello, R. Carli, L. Schenato, and M. Todescato, "A partition-based implementation of the relaxed ADMM for distributed convex optimization over lossy networks," in *Proc. IEEE Conf. Decis. Control (CDC)*, Dec. 2018, pp. 3379–3384.
[26] I. Notarnicola, R. Carli, and G. Notarstefano, "Distributed partitioned big-data optimization via asynchronous dual decomposition," *IEEE Trans. Control Netw. Syst.*, vol. 5, no. 4, pp. 1910–1919, Dec. 2018.
[27] R. Carli and G. Notarstefano, "Distributed partition-based optimization via dual decomposition," in *Proc. 52nd IEEE Conf. Decis. Control*, Dec. 2013, pp. 2979–2984.
[28] *UCTE Operation Handbook*, UCTE, Brussels, Belgium, 2004.
[29] M. Chenine, K. Zhu, and L. Nordstrom, "Survey on priorities and communication requirements for PMU-based applications in the Nordic region," in *Proc. IEEE Bucharest PowerTech*, Jun. 2009, pp. 1–8.
[30] K. Zhu, M. Chenine, L. Nordström, S. Holmström, and G. Ericsson, "Design requirements of wide-area damping systems—Using empirical data from a utility IP network," *IEEE Trans. Smart Grid*, vol. 5, no. 2, pp. 829–838, Mar. 2014.
[31] *Benchmark Systems for Network Integration of Renewable and Distributed Energy Resources*, document CIGRE Task Force C6.04.02, 2014.

MARC MORITZ received the M.Sc. degree in electrical engineering from RWTH Aachen University, Aachen, Germany, in 2022, where he is currently pursuing the Ph.D. degree with the Institute for Automation of Complex Power Systems, E.ON Energy Research Center. He is also a Research Associate with the Institute for Automation of Complex Power Systems, E.ON Energy Research Center, RWTH Aachen University. His research interests include HVdc converter control, control of converter-driven power systems, and harmonic stability.

TOBIAS HEINS received the M.Sc. degree in electrical engineering from RWTH Aachen University, Aachen, Germany, in 2020. He is currently a Research Associate with the Institute for Automation of Complex Power Systems, E.ON Energy Research Center, RWTH Aachen University. His research interests include control, stability, modeling, and analysis of converter-driven power systems.

SRIRAM KARTHIK GURUMURTHY (Graduate Student Member, IEEE) received the M.Sc. degree in electrical power engineering from RWTH Aachen University, Aachen, Germany, in 2017. He is currently a Research Associate with the E.ON Energy Research Centre, Institute for Automation of Complex Power Systems, RWTH Aachen University. His research interests include modeling, control, stability analysis, and automation of power electronics-driven power systems.

MARTINA JOŠEVSKI (Member, IEEE) received the Ph.D. degree in mechanical engineering from RWTH Aachen University, Aachen, Germany, in 2018. From 2018 to 2021 she was a Postdoctoral Research Associate with the E.ON Energy Research Center, Institute for Automation of Complex Power Systems, RWTH Aachen University, where she was leading the Team for Advanced Control Methods in Power System Applications. She is currently a Lead Research Engineer and the Project Manager with Eaton Research Labs, Eaton Corporation, where she is coordinating research activities related to novel power conversion technologies and supporting digital services. She is also active as an external Lecturer with RWTH Aachen University. Her research interests include the modeling of dc and hybrid power systems, optimal control of low-inertia power systems, and distributed optimization with a specific focus on model predictive control.

ILKA JAHN (Member, IEEE) received the B.Sc. and M.Sc. degrees in electrical engineering from RWTH Aachen University, Germany, in 2012 and 2015, respectively, and the Ph.D. degree in electrical engineering from the KTH Royal Institute of Technology, Sweden, in 2021. In 2015, she was with ABB Corporate Research, Sweden. From 2022 to 2024, she was the Junior Research Group Leader with the Institute for Automation of Complex Power Systems, RWTH Aachen University. In June 2024, she will be an Assistant Professor with the KTH Royal Institute of Technology. Her main research interests include the control and protection of HVdc systems, power systems dominated by power electronic converters, and innovative software solutions.

ANTONELLO MONTI (Senior Member, IEEE) received the M.Sc. degree (summa cum laude) and the Ph.D. degree in electrical engineering from Politecnico di Milano, Italy, in 1989 and 1994, respectively. He started his career with Ansaldo Industria and then moved to Politecnico di Milano, as an Assistant Professor, in 1995. In 2000, he joined the Department of Electrical Engineering, University of South Carolina, Columbia, SC, USA, as an Associate Professor and then a Full Professor. Since 2008, he has been the Director of the Institute for Automation of Complex Power Systems, E.ON Energy Research Center, RWTH Aachen University. Since 2019, he has also been a double appointment with Fraunhofer FIT, where he is currently developing the new Center for Digital Energy, Aachen. He is the author or coauthor of more than 400 peer-reviewed papers published in international journals and the proceedings of international conferences. He was a recipient of the 2017 IEEE Innovation in Societal Infrastructure Award. He is an Associate Editor of *IEEE Electrification Magazine*, a member of the editorial board of *Sustainable Energy, Grids and Networks* (Elsevier), and a member of the founding board of *Energy Informatics* (Springer).